Build orientation, surface roughness, and scan path influence on the microstructure, mechanical properties, and flexural fatigue behavior of Ti-6Al-4V fabricated by Electron Beam Melting

Andrew H. Chern[1*]
Peeyush Nandwana[2]
Robert McDaniels[3]
Ryan R. Dehoff[1,2]
Peter K. Liaw[4]
Robert Tryon[3]
Chad E. Duty[1]

[1] Department of Mechanical, Aerospace, and Biomedical Engineering, The University of Tennessee, Knoxville, TN, United States
[2] Deposition Science and Technology Group, Oak Ridge National Laboratory, Knoxville, TN, United States
[3] VEXTEC Corporation, Brentwood, TN, United States
[4] Department of Materials Science and Engineering, The University of Tennessee. Knoxville, TN, United States

*Corresponding author, E-mail: achern@vols.utk.edu

ABSTRACT

In the present work, microstructure and fatigue behavior of Electron Beam Melted (EBM) Ti-6Al-4V have been systematically studied. Fatigue behavior was investigated using four-point bend tests of rectangular bars with internal features fabricated with different build orientations, scan paths, and surface conditions. Microstructural variations were evaluated by optical microscopy and Vickers micro-hardness indentations, both of which were found to be consistent throughout the build and within ranges reported in the literature. The fatigue performance of the EBM material was comparable to wrought Ti-6Al-4V when the loading direction was parallel to the build direction, but severely limited when loaded perpendicular to the build direction or if surface roughness defects were present. Scanning electron microscopy and interrupted fatigue tests were utilized to characterize fracture surfaces, failure mechanisms, crack initiation, and propagation behavior. Crack initiation sites in the vertically-oriented specimens were identified to be melt-related defects formed by insufficient melting.

Keywords: Electron Beam Melting, Titanium, Fatigue, Surface Roughness, Defects

1. Introduction

Additive manufacturing (AM) allows for the fabrication of complex geometries, such as fine meshes [1], directly from a computer file that would be difficult or impossible to produce by traditional means. Electron beam melting (EBM) is one such technology that is of high interest to the aerospace, biomedical, and energy industries. A primary advantage of the EBM process is that deposition occurs inside a vacuum build chamber at elevated temperatures, reducing the residual stresses incurred by rapid solidification [2]. Furthermore, while other metal AM processes are carried out under inert atmosphere, the build chamber in EBM is first pumped to a pressure of about 5e-5 mbar and then backfilled with He to maintain a pressure of 0.005 mbar during the build, which is advantageous for reactive metals like Ti alloys.

The dual phase titanium alloy, Ti-6Al-4V, is often employed for aerospace structural applications where high strength and fatigue damage tolerance are needed because of its superior strength to density ratio, corrosion resistance, and toughness [3, 4]. The widespread use of Ti alloys is limited because of difficulties in machining, cost, and low recyclability [5]. Buy-to-fly ratios, the ratio of the stock materials weight to the weight of the finished component, can be as high as 33:1 for some aerospace structural components [6], meaning a great amount of material can be lost as waste chips from machining. The utilization of the EBM technology presents the opportunity to reduce the buy-to-fly ratios, wasted material, increase productivity and performance.

Considering the clean build environment, elevated build temperatures, design freedom, and ability to reduce buy-to-fly ratios, the EBM technology is well suited for application within the aerospace industry. However, the industry's renowned dedication to safe operations and conservative design criteria requires parts to be backed with strong quality assurance. Therefore, a fundamental understanding of the fatigue-damage tolerance, underlying mechanisms, and

impact of processing conditions is required for the use of EBM technology for critical flight components and its potential fully realized [7, 8].

Recent works [6, 9, 10] have indicated that components in the as-fabricated condition often meet ASTM Standards [11] for tensile properties. The fine colony and Widmanstätten microstructures characteristic of EBM-processed Ti-6Al-4V [12, 13] provide sufficient mechanical properties for many applications. However, fatigue performance of the as-fabricated Ti-6Al-4V falls short of the traditionally-manufactured material due to the surface roughness [10, 14, 15] and porosity [16-18] inherent to the EBM process. Comparable fatigue performance can be obtained after via hot isostatic pressing (HIP) and machining [15, 19], but HIP coarsens the microstructure and reduces tensile strength [20] and machining adds costs as a post-fabrication finishing process. To realize the full benefits of EBM fabrication, documentation and analysis of the fatigue properties in the as-deposited condition are needed.

In the present work, rectangular Ti-6Al-4V samples were fabricated with an Arcam Q10 machine in different orientations and then subjected to four-point bend loading. At the time of publication, the fatigue data of the EBM components is limited to axial fatigue [10, 14, 16, 17, 19, 21], 3-point bend [22], and 4 point bend loading with test samples using simple geometries (*i.e.,* no internal features) [23]. Kahlin et al. suggested that the fatigue behavior of rough as-fabricated surfaces and notched components be investigated as very few aircraft components have simple geometries without corners, radii, or stress concentrations [15]. However, there are limited studies in the open literature investigating fatigue behavior of test specimen with internal features incorporated into the original build. Günther et al. [24] investigated the fatigue behavior of selective laser melted specimen with internal channels and found that fatigue cracks initiated predominantly at the rough surfaces of the internal channels. The rectangular test specimen in the present study had internal features in the form of two small (0.79375 mm, 1/32 inch) diameter holes. This dimension was chosen such that two symmetrical holes could be placed within the span of the inner pins where the bending moment and surface stress is constant.

The majority of fatigue data currently available in the literature is based on axial-fatigue tests, which may not be representative of fatigue behavior of service parts. As an example, Edwards et al. [16] showed that wrought Ti-6Al-4V outperformed the EBM as-deposited material in laboratory testing, but EBM-fabricated brackets survived multiple lifetimes under the designed loading conditions. This result motivates the need to subject EBM-fabricated components to different loading conditions and study the fatigue behavior of samples that are more representative of in-service parts while still producing enough replicates to make statistically-relevant conclusions. This work assesses the failure mechanisms and flexural fatigue strength of EBM Ti-6Al-4V and correlates the results to the EBM process, microstructure, and defects. Four-point bending fatigue was chosen as it is a convenient method for studying crack initiation, early crack growth, and allows for the interruption of tests for microscopic observation [25]. Test coupons in this study were fabricated with internal features and subjected to four-point bend loading in the as-deposited material condition. Interrupted fatigue tests were performed so that crack initiation and propagation behavior of EBM Ti-6Al-4V could be evaluated.

2. Materials and Methods

2.1 Ti-6Al-4V Powder and Specimen Fabrication

An Arcam Q10 EBM (Arcam EBM, a GE Additive Company, Mölndal Sweden) machine at the Manufacturing Demonstration Facility of the Oak Ridge National Laboratory (software control version 5.0.104, layer thickness of 50 μm, melting current of 28 mA, accelerating voltage of 60 kV) was used to fabricate blocks (Figures 1a and 1b) on a 210 mm × 210 mm stainless steel build plate. Gas atomized spherical Ti-6Al-4V powder supplied by Tekna was to manufacture the samples. The powder had a mean particle diameter of 81.78 μm +/- 21.7 μm with D10, D50, and D90 numbers of 59.2, 79.0, and 107. 4 μm, respectively (measured with a Horiba LA950 analyzer). Images of the powder at both 80x (Figure 2a) and 120x (Figure 2b)

magnification were acquired using a HITACHI TM3030 SEM operated at 15kV. Powder chemistry, analyzed by Luvak Inc. (Boston, MA) (6.53 (wt.%) Al, 4.05 V, 0.190 Fe, 0.107 O, 0.02 C, 0.017 N, 0.003 H) was found to adhere to ASTM F2924-14 [26]. Oxygen, hydrogen, and nitrogen were measured by inert gas fusion. Carbon was measured by combustion infrared detection, and all other elements were measured by direct current plasma emission spectroscopy. All blocks were fabricated in a single build and specimens for fatigue, microhardness, and metallography were extracted from these. All baseline mechanical and fatigue properties were evaluated using as-fabricated material (*i.e.,* no post-process heat-treatments nor HIP).

EBM Process Parameters used to fabricate the Ti-6Al-4V blocks are detailed in Table I. Each layer was melted using the Arcam standard preheat-contour-hatch melting procedure. Block 1 had dimensions of 115 mm × 64 mm × 69.75 mm (length × width × height). The blocks positioned on the left and right side of the build plate, Blocks 2 and 3, had dimensions of 122.5 mm × 21 mm × 61.5 mm. The blocks located on the front and back of the plate, Blocks 4 and 5, had dimensions of 194 mm × 21mm × 61.5 mm. The block dimensions were chosen to maximize the amount of sample replicates while allowing for the fabrication of samples with different orientations and scan paths. Blocks 1, 4, and 5 had two 0.79375 mm holes located off center with 5.08 mm spacing fabricated in the original build. The total build time, including cool down, was 28 hours and 13 minutes. Thorough descriptions of the Arcam EBM process and hardware are provided elsewhere [27-29].

2.2 Microstructural Analysis

Metallographic analysis was conducted to observe the microstructure in different orientations (*i.e*., the XY plane is parallel to the build plate, and the Z plane is perpendicular to the build plate). Samples for metallographic analysis were sectioned from the front block, mounted in conductive mounting material, mechanically ground using SiC papers, and final polished using a 0.04 μm colloidal silica suspension on a MD-Chem (Struers, Cleveland, OH) polishing pad. The

polished samples were then etched using Kroll's reagent (100 mL water, 6 mL HNO3, and 3 mL HF). A Leica DM4000 optical microscope was used to image the microstructure and the α lath thickness was measured using the Vander Voort method [30].

2.3. Mechanical Testing

Vickers microhardness indentations were taken from three locations in the build. Samples were sectioned approximately 6 mm in the Z-direction from the top of the build (denoted 'Top Build'), approximately 38 mm from the build plate in Block 1 and 25.4 mm from the build plate in Block 3 (denoted 'Mid-Build'), and approximately 6 mm from the build plate ('Bottom Build') from both Blocks 1 and 3. The samples were prepared using the same techniques described above, but without etching. Two different orientations were evaluated from each sampled area denoted 'XY' (the plane parallel to the build plate) and 'Z' (the plane perpendicular to the build plate). Nine measurements were taken on each sample in a 3×3 grid pattern spanning the sample. The microhardness measurements were performed on a Wilson VH1202 Vickers Hardness Tester at a load of 500 gf applied for a 15 second dwell time at room temperature.

Samples for tensile testing were also machined, prepared, and tested, but due to geometric and machining limitations, the tensile tests were not to ASTM E8 standards [31]. The tensile bars machined in this work had a gauge length of just 9.5 mm and overall length of 63.5 mm while E8 Sub-size Specimen require a gauge and overall length of 25 mm and 100 mm, respectively. A more detailed description on the preparation, sample dimensions, test methods, and results is provided elsewhere [32] and excluded from the present work.

2.4. Four-Point Bend Fatigue Testing

Specimen for four-point bend (4PB) fatigue testing were machined from the larger blocks to final dimensions provided in Figure 3a. The machining process included first rough cutting with either an OMAX 2626 Water Abrasive Machining Center or wire electrical discharge machine

(EDM) and then milled to final dimensions. After machining, the specimen's face that experiences tensile stresses during loading was mechanically ground and polished with a 3-μm diamond suspension slurry. The side surfaces of the test specimen were either left in the as-fabricated condition or were machined and fine ground (Figure 3b). The side surfaces were fine-ground where the final SiC paper was at least 1200 grit to eliminate surface imperfections as suggested in [33]. To investigate possible anisotropy in the fatigue behavior, test specimens were cut from Block 2 (Figure 1a) such that the specimen's long axis was either perpendicular or parallel to the build plate and denoted as 'vertical' and 'horizontal' specimens, respectively. Figure 3c is a schematic indicating the test specimens' orientation with respect to build direction.

The load-controlled four-point bend fatigue tests were performed on an MTS 810 servo-hydraulic test machine with a load ratio R = P_{min}/P_{max} of 0.1 at a load frequency of 5 Hz, where P_{min} and P_{max} are the maximum and minimum loads, respectively. The maximum tensile stress within the span of the two outer pins was calculated using Equation 1 derived using the beam theory of engineering mechanics [34].

$$\sigma_{tensile} = \frac{3P(S_o - S_i)}{2wt^2} \qquad (1)$$

where P is the applied load, S_i denotes the inner pin spacing, S_o is the outer pin spacing, t is the thickness of the sample, and w is the width of the sample. For the samples tested in this study, the inner pin spacing (S_i) was 10 mm, outer pin spacing (S_o) was 40 mm, sample thickness (t) was 6.35 mm, and width (w) of 20.32 mm. The dimensions where chosen to satisfy the inner pin spacing to sample thickness ratio (S_i/t) and outer pin spacing to inner pin spacing (S_o/S_i) ratio for constant stress distribution as suggested [25]. A specimen failure was defined when the machine limits exceeded a displacement of 1.27 mm. Experimental 4PB fatigue test set up of both vertically- and horizontally-oriented samples is shown schematically in Figure 4. Fracture surfaces

and fatigue-crack-initiation sites were imaged using a Zeiss EVO MA15 scanning electron microscope (SEM) operated at 20.0 keV.

Interrupted fatigue tests were conducted on selected vertical and horizontal fatigue samples to observe crack initiation and propagation behavior. During the interrupted tests, the cyclic loading was stopped at various cycle intervals and the surface cracks were imaged and measured using a Keyence VHX 5000 digital microscope. The cycle counts at which to interrupt the tests were chosen based off completed test results and estimated cycle count to failure.

Because of different design needs and capabilities, the internal features were studied under different conditions. Three separate methods were used to fabricate the 0.79375 mm diameter holes to present a variety of surface and fabrication conditions. For applications where machining of internal features may not be possible, the internal features of some test specimens were studied in the as-fabricated condition. The minimum feature size of an EBM machine is reported to be 0.1 mm with a geometric tolerance of +/- 0.2 mm [35, 36], thus the holes were expected to be within the fabrication limits of the Arcam machine. These features were included in the original build of Block 4 and are referenced within this study as ‘as-built’ holes. For applications where a limited amount of machining is needed, several specimens with ‘as-built’ holes were selected, and the holes were reamed to the final 0.79375 mm diameter. These specimens are referred to as ‘reamed’ holes. This method of hole fabrication will also interrupt the scan path used to manufacture the holes during the EBM process and can also influence solidification gradients. The final hole condition, ‘machined’ holes, denotes holes that were conventionally drilled to final dimensions through solid material. These specimens were sectioned from Blocks 2 and 3.

For comparison purposes, conventionally manufactured wrought plate Ti-6Al-4V Extra Low Interstitials (ELI) specimens were also prepared for Vickers hardness measurements and four-point bend fatigue tests by the same methods. The wrought Ti-6Al-4V ELI was supplied by

RTI International Metals Inc. in plate form and met ASTM F-136 [37] and B-265 [38] for chemical composition and mechanical properties, respectively. For all materials, orientation, and hole conditions, at least 3 fatigue tests were conducted.

When statistically significant comparisons could be made, one-way analysis of variance (ANOVA) tests were conducted on the mean fatigue lives at the 95% confidence interval ($\alpha = 0.05$) using Minitab Statistical Software version 18 (Minitab Inc., State College, Pennsylvania).

3. Results

3.1 Microstructural Analysis

The microstructure of the Ti-6Al-4V fabricated by the EBM process in this study consisted of a continuous fine structure of α/β lamellae with Widmanstätten and colony morphologies (Figures 5a – 5d). Columnar prior-β grains extended multiple layers in the build direction. This type of microstructure is typical of EBM builds due to the rapid quench from melt followed by *in-situ* anneal. Martensite (α´) was not observed in the microstructure. The average α lath width was measured to be 2.93 +/- 0.83 μm, within the range (0.66 μm – 4 μm) reported in the literature for EBM Ti-6Al-4V [39-41]. The microstructure in the present study showed a slightly coarser microstructure than other EBM-fabricated components due to the thick wall widths which were greater than 20 mm.

Melt related lack-of-fusion (LOF) defects and gas pores were readily observed (Figures 6a and 6b, respectively) throughout the build. The observed lack-of-fusion defects are located in between layers and oriented perpendicular to the build direction and result from un-melted packets of powders that received insufficient energy during fabrication [42]. Gas pores, the distribution of which can be dependent on the scan strategy [43], were also observed and are thought to be artifacts of the gas-atomization process used to manufacture the powder.

3.2. Vickers Micro-Hardness Measurements

To document effects of the initial cooling rate from β to α phase fields and subsequent *in-situ* annealing on α lath size, Vickers micro-hardness measurements as a function of the build height, orientation, and block size are provided in Figure 7. The Vickers micro-hardness of the EBM material varied from 304 to 388 HVN, but on average was consistent throughout the build and within the range reported in the literature [40, 44, 45]. The average hardness of Block 1 was 332.8 +/- 6.5 HVN and Block 3 was 334.0 +/- 5.6 HVN. Blocks 2 and 3 had a wall thicknesses of 21 mm and similar hardness of parts with wall thickness of 20 mm (330 HVN) [46]. Although the part size has been related to microstructure where thin-walled structures experience a higher cooling rate and finer microstructure [40], Block 1, with a wall thickness of 64 mm, displayed similar hardness to Block 3 despite a larger wall thickness.

3.3. Four-Point Bend Fatigue Tests

The mean fatigue lives and standard deviations of all material, orientation, surface, and hole conditions are provided in Figure 8 and summarized in Table II.

3.3.1. Surface Roughness

Comparisons between Groups 1 – 3 show that the EBM samples with rough surfaces, either along the sides of the samples or within the bore of the hole (as shown in Figures 9a, 9b, 10a, and 10b) displayed lower mean fatigue lives than their machined counterparts (Group 1 = 16,195 +/- 670 cycles, Group 2 = 20,920 +/- 3,225 cycles, Group 3 = 26,909 +/- 7,521 cycles). Sun et al. suggests a 650 μm depth of cut to remove all surface roughness defects. However, to remove all surface defects in the present work, a 725 μm depth of cut was required. The rough as-fabricated surface of EBM components is characterized by sharp interfaces resulting from melt-pool overflow and partially-sintered powders (Figures 10a and 10b) and similar to the

surfaces in other studies in the literature [10, 22, 47-49], which provides favorable crack initiation sites and greatly reduces the fatigue resistance. As others [24, 50] have suggested, the low scatter in Group 1 (As-Built Surface/As-Built Hole) indicates that fatigue crack initiation occurs early in the test and the fatigue life of the specimen with as-fabricated surfaces is dominated by crack propagation.

On samples with as-fabricated outside surfaces, multiple cracks were observed to initiate at the outer edge surface as opposed to the machined hole. The stress concentration factor (SCF) of an EBM as-fabricated surface was measured to be as high as 9.1 [51]. In comparison, the SCF a rectangular plate with similar geometry under pure bending was estimated to be 2.7 [52]. This difference in SCF indicates that the rough as-fabricated surface can be more detrimental to fatigue than internal machined features which act as stress concentrators in aerospace components [53].

Samples in Groups 1 – 3 were subjected to slightly different stress levels. Thus, a direct statistical comparison is not possible. However, general conclusions can still be made as the groups with rougher surfaces (Group 1 and 2) were tested at lower stresses and still failed earlier than those tested at a higher stress with machined surfaces (Group 3). These experiments demonstrate the detriment the rough EBM surface has on fatigue performance.

3.3.2. Scan Path

Among the samples that had machined outer surfaces, a direct comparison was made between samples with ‘machined holes’ (Group 5) and samples with ‘reamed holes’ (Group 4). As mentioned previously, the ‘reamed holes’ were drilled to a final diameter of 0.79375 mm from undersized holes produced during the EBM process. Thus, the beam scan path of the samples with ‘reamed’ holes was different than the scan path used to fabricate the samples with ‘machined’ holes. An increase in the porosity distribution near the ‘reamed hole’ was expected since pores have a tendency to accumulate at the end of hatch infill scans [43, 54] but SEM fractography did

not reveal a notable difference in the near-hole porosity distribution for either set of samples. However, the fatigue performance between the two sample sets showed a statistically-significant difference (*i.e., p* < 0.05) based on an ANOVA test with $F = 46.42$, $p = 0.002425$. The lower average fatigue life in the 'reamed' specimen (Group 4 = 30,207 +/- 3,367 cycles, Group 5 = 45,759 +/- 7,255 cycles) was attributed to the rough surface finish within the hole. Reaming the partial holes to final dimension was effective for removing partially-sintered powders, but surface cavities remained along the bore of the 'reamed' sample (Figure 10c). The reaming did not sufficiently remove the rough surface left over from the EBM build process despite expanding the undersized hole to the required diameter. Surface roughness within fastener holes has been correlated to lower fatigue lives by others [53, 55]. Therefore, the surface defects in the 'reamed' specimen acted as stress concentrators and decreased fatigue resistance. Machining marks were observed in 'machined' samples, but no lack-of-fusion or gas porosity defects were exposed during drilling.

When comparing samples machined from blocks with different original volumes (Group 5 = Block 2, Group 6 = Block 1), ANOVA test results of $F = 0.45$, $p = 0.532$ indicated no statistically-significant difference in fatigue performance (Group 5 = 45,759 +/- 7,255 cycles, Group 6 = 48,731+/- 1,856 cycles). Both sets of samples were oriented horizontally with machined surfaces and machined holes. Since the Vickers micro-hardness measurements of both blocks were similar, the microstructures were considered roughly equivalent, and thus the similar fatigue properties were expected.

3.3.3. Build Orientation & Comparison to Wrought Plate Ti-6Al-4V ELI

Fatigue lives of samples built in different orientations were compared, each having machined outer surfaces and machined holes. The average fatigue life of the horizontally-oriented samples (45,759 +/- 7,255 cycles) was about 2x that of the vertically-oriented (26,909 +/- 7,521 cycles) samples, a statistically-significant difference (ANOVA test resulted with $F = 14.39$, $p =$

0.007). The difference in the fatigue life was attributed to multiple crack initiation sites observed near the surface of the vertically-oriented specimens.

The horizontally-oriented samples (Group 5) showed a comparable fatigue performance to the conventionally manufactured wrought Ti-6Al-4V ELI as the ANOVA test results of $F = 2.69$, $p = 0.176$ indicated no statistical difference in mean fatigue lives (Wrought = 49,464 +/- 7,688 cycles, Group 5 = 45,759 +/- 7,255 cycles, Group 6 = Group 6 = 48,731+/- 1,856 cycles). Failure mechanisms were similar as fatigue cracks initiated at the machined hole in both horizontal-EBM and wrought Ti-6Al-4V samples.

3.3.4. Interrupted Fatigue Tests

A summary of the results from the interrupted fatigue tests is provided in Figure 11 and Table III. A 'Failure Crack' was considered the crack which propagated to the edge first. To obtain the crack length at failure, the final crack length measurement in Figure 11 was assumed to be half the sample width. The cycle count at failure of the respective sample was then assigned to this length. Two cracks were observed initiating from a single hole in Vertical Sample 2 and propagating at nearly equal rates in different directions. Crack 1 propagated towards the front of the sample and Crack 2 towards the back, thus, both measurements are reported. In all horizontal samples, the crack that initiated first was the Failure Crack.

Observation of Figure 11 reveals that cracks initiated earlier in vertically-orientated samples than in the horizontally-oriented samples. Although the Failure Cracks initiated from a hole in Vertical Sample 2, cracks were observed initiating along the polished surface before initiating at the machined hole in both vertical samples. These crack initiation sites, inspected by digital microscopy and SEM fractography, were found to be LOF defects that either intersected the surface or were near sub-surface (Figures 12a -12c). Figure 12c shows the Failure Crack of Vertical Sample 1 initiating from a LOF defect that was exposed to the surface during machining

and polishing. Powder particles can be observed within the defect when microscopically inspected. Surface cracks in the vertical specimen were observed as early as 7,000 cycles while cracks in the horizontal specimen were not observed until at least 20,000 cycles. The cracks in the horizontal specimen were only observed to initate from the machined hole as shown in Figure 13 rather than surface defects.

4. Discussion

4.1 Vickers Micro-Hardness

The influence of grain size on mechanical properties, such as yield strength and indentation hardness, can be quantified through variations of the Hall-Petch equation [56-58]. A number of authors [59, 60] report that the Vickers hardness is inversely proportional to the square root of the lamellar spacing in traditionally manufactured (*i.e.,* methods other than AM) Ti-6Al-4V. A Hall Patch type equation for hardness and yield strength of EBM Ti-6Al-4V was first reported by Jamshidinia et al. [61] and an empirical model between α lath thickness and hardness was later proposed by Galarraga et al. [62] and provided in equation 2:

$$HV = 307 + 44 * \frac{1}{\sqrt{\delta_{\alpha\, lath}}} \quad (2)$$

where, *HV* is the Vickers micro-hardness and $\delta_{\alpha\, lath}$ the α lath thickness in μm. The experimentally obtained Vickers micro-hardness values and equation 2 were utilized to back-calculate the α lath thickness. Inputting the average Vickers micro-hardness values (average hardness of Block 1 was 332.8 +/- 6.5 HVN, Block 3 was 334.0 +/- 5.6 HVN), the calculated lath thickness values of 2.66 and 2.92 μm for Block 1 and Block 3, respectively, were obtained. These calculated values correlate well with the measured lath width. By these calculations and observations, the average lamellar spacing appears to be consistent regardless of the wall thickness, build orientation, and distance from the build plate in this build. However, the lath thickness was shown to increase over

lesser distances (a 25-mm distance from the build plate) [63] and thinner wall thicknesses (from 1 mm to 20 mm) [64] reported in other EBM analyses in the open literature.

The Hall-Petch model presented in Equation 2 accurately correlates Vickers micro-hardness with α lath thickness. However, the model does not consider other factors which can influence the micro-hardness of Ti-6Al-4V. This could include oxygen content [65, 66], amount of α phase present [67], and texture of α phase [68]. Review of Figure 7 reveals the scatter in the HVN data for 'Mid-Build' XY-plane for both Block 1 and Block 3 is greater than the others with a standard deviation of 22 HVN. This scatter occurs different layer heights as there exists a roughly 12.6 mm difference in Z-height between 'Mid-Build of Block 1 and Block 3. Review of the beam current and bottom temperature in the build log file did not reveal anomalies over this section of the build. Possible sources of the scatter could include indenting on prior β grains, indenting near or into a subsurface pore, or differences in local α phase texture. Scatter in HV data of similar range was reported for as-fabricated [39] and heat treated [62] EBM Ti-6Al-4V.

4.2. Surface Roughness

It is well documented in the open literature that surface roughness has a deleterious effect on fatigue resistance [14, 22, 47, 69-71]. The valleys on a rough surface serve as stress concentrations which induce different levels of fatigue crack nucleation [72]. In general, decreasing the roughness through post-process machining, grinding, or polishing results in increased fatigue life [47, 73, 74]. This was observed in the present study as the machined samples generally displayed better fatigue resistance than samples with as-fabricated surfaces. The layer-by-layer fabrication of powder bed fusion produces rough surfaces which are different than those obtained through traditional manufacturing methods. Both solidification of the melt pool (often referred to as 'primary roughness') and partially melted powder ('secondary roughness') contribute to the overall roughness [47, 48, 75]. Primary roughness, marked by peaks and valleys

formed by melt pool overflows, governs fatigue behavior while secondary is not a significant factor [48]. The primary roughness must be completely removed for fatigue improvements as the deep valleys acts as stress concentrators and early crack initiation sites. The reaming operation performed on Group 4 (reamed holes, horizontal orientation) in the present study did not completely remove the primary roughness (Figure 10c) and the observed fatigue life was inferior to Group 5 (machined holes, horizontal orientation). The depth of cut required to remove this primary roughness, 650 μm suggested by Sun et al. [49] and 725 μm suggested in the present, must be considered when designing components for fatigue applications.

Non-traditional methods of machining, such as chemical etching [49, 76], have been investigated as approaches for smoothening roughness where machining is not possible. The results of this study indicate that if internal geometries are to be machined (whether by traditional or using non-traditional methods), enough material must be removed, and a uniform homogeneous surface must be achieved in order to increase the fatigue tolerance of a component with internal features.

Average roughness from a median line (R_a) and average difference between a peak and valley (R_z) are widely reported in the literature and used for quality control purposes, but do not consider the depth of the notches independently. Thus, R_a and R_z measurements can be skewed by secondary roughness or not capture the severity of the surface notches most detrimental to fatigue. For quality control of EBM materials required in the aerospace industry, a new surface roughness metric is needed to correlate fatigue resistance to surface roughness. R_{vm} (maximum surface roughness) is suggested such that the depth of the valley is properly considered [51].

4.3. Defects and EBM Scan Parameters

4.3.1. Origin of Anisotropic Fatigue Behavior

In the present study, fatigue cracks initated by different mechanisms depending on the build orientation resulting in aniostropic fatigue behavior. The vertically-oriented samples, in which the build layers are oriented such that the inter-layer LOF defects are perpendicular to the surface under tensile stresses, failed by layer delamination where existing LOF defects are opened by the bending load. The LOF defects that intersected the surface or near the surface concentrated stress and provided favorable crack-initiation sites. In contrast, the horizontal samples failed by through-thickness crack propagation by cracks initiated at the machined hole. In a horizontally-oriented specimen, a single build layer is exposed to the maximum tensile stress and any defects were eliminated by polishing. The LOF defects in the horizontally-oriented samples were aligned such that the long axis of the defect was oriented parallel to the polished surface (surface in tension), and thus had little effect on the fatigue life. Chastand et al. [77] suggested that the orientation of the LOF defects gave parts built in the XY-direction (horizontal) better fatigue properties than those built in the Z-direction (vertical). The results of the present work confirm this assumption that the LOF defects orientated perpendicular to stress direction were more critical to fatigue.

4.3.2. EBM Scan Parameters

An Arcam internal algorithm, known as the "*Current Compensation Function*", calculates the beam current for a given scan as a function of the scan line length such that the difference required in the input beam power can be accounted for when melting small and large areas [29]. The *Current Compensation Function* modifies the input current according to Equation 3 [29] i_{melt}

$$= i_{input} * \left(1 + PropK * \frac{l - l_{Ref}}{l_{Ref}}\right) \quad (3)$$

where i_{melt} is the current used during the hatch melt, i_{input} is the current set by the user in the process Themes, *PropK* is a proportionality constant, l_{Ref} the reference scan length, and *l* the length of the line to be melted according to the geometry. If multiple parts have non-melted area

in between, all melt segments of the same line are added to calculate the scan length of that beam scan path, as shown schematically in Figure 14. All 5 blocks in the present study were uploaded as a single **.stl* file and assigned a single melt theme so the scan length calculated in the X direction is the sum of the ΔX_n segments indicated by the blue arrows and the scan length in the Y direction is the sum of the ΔY_m segments indicated by the red arrows (Figure 14). The part geometry and Theme/Model assignment influence the energy of the beam used in the melt and thus the resulting microstructure and defects. The effects of the beam scan length and its effects on microstructure, mechanical properties, and defects have been documented in the literature for various EBM manufactured alloys [17, 78, 79]. The algorithm calculates a greater current value for longer scan lengths, but the value is bounded by the *Maximum Current* value. If the calculated current needed to sufficiently melt a line exceeds the *Max Current* value, the *Max Current* will be used rather than the calculated value and the line may receive insufficient energy for complete melting. Arcam recommends maximum scan lengths of 90 – 100 mm to avoid insufficient melting [78, 80]. The number of scans within a range of lengths (in mm) is output in the Arcam build log file. Figure 15 provides the sums of the lengths above the recommended 90 mm maximum value from the current build. A total of 151,194 scans were greater than the Arcam recommended value and likely received insufficient energy for complete melting. The lack-of-fusion defects that acted as fatigue crack initiation sites in the vertically-oriented samples were likely a result of this insufficient melt current and energy input.

A number of build design practices have been suggested in the literature to ensure that lack of fusion melt defects are avoided when using the Arcam *Current Compensation Function*. It was suggested to orient parts vertically to unsure the shortest scan length [80]. However, anisotropic fatigue behavior attributed to notch-like surface roughness defects has been observed in as-fabricated EBM Ti-6Al-4V where the vertically-oriented parts had lower fatigue strength [73, 81]. Orienting a part to minimize scan lengths could be a viable method if post-processing

eliminates these surface roughness defects. Reducing the effective scan length by assigning models separate melt *Themes* is also a good build practice as suggested in [17]. By this method, even if the *Themes* are identical, the parts are not treated as a single entity. A build can then be simulated in EBM Control to ensure all scan lengths are below the recommended 90 mm length.

4.4. Mitigation of Defects

Although the fatigue performance of the horizontally-orientated EBM Ti-6Al-4V (machined and polished surfaces) displayed comparable fatigue performance to the wrought plate Ti-6Al-4V, actual service parts are often more complex and experience multiple loading conditions during service [47]. If the direction of loading was altered, the fatigue life of the horizontally-oriented samples would likely be limited by the presence of the LOF defects (similar to vertically-oriented samples). To account for such variability, a post-fabrication process such as hot isostatic pressing (HIP) can effectively eliminate these defects. However, the HIP process is ineffective for defects that intersect a free surface [15]. Because machining and polishing can expose LOF defects, it is recommended that a HIP process is performed prior to machining. If parts were machined prior to HIP, the fatigue performance could be reduced as the elevated temperatures utilized in HIP would coarsen microstructure and reduce strength [20] and favorable crack initiation sites exposed from machining.

In addition to the non-spherical melt defects, spherical pores (Figure 6b), the presence of which is credited to the powder feedstock as an artifact of the gas atomization (GA) process [82-84], were observed throughout the build. Although the LOF defects were observed to be more detrimental to fatigue in the present work, the gas pores have also been reported to be early fatigue crack initiation sites in as-fabricated material [16, 20]. Although detected after HIP, the size of gas pores is largely reduced as review of the open literature revealed that gas pores are between 1.5 μm and 5 μm in diameter following a HIP cycle, a finding based on the resolution of μXCT scans [84-86]. Unlike the LOF defects, gas pores are filled with an insoluble gas and shrink

after HIP (not eliminated like LOF defects) and are susceptible to expansion after subsequent heat treatments or high-temperature applications [84, 87]. The use of plasma rotating electrode process (PREP) powder (highest density and lowest amount of porosity) can reduce the percentage of pores in the finished component by addressing porosity at its source rather than mitigating the matter post-EBM fabrication.

Although there are clear benefits to HIP as EBM manufactured Ti-6Al-4V displays comparable fatigue strength to conventional material following a post-process HIP cycle and machining [73], it is a costly procedure, adds a post-processing step, and coarsens microstructure that reduces material strength [18-20]. Considering that the most detrimental defects to fatigue result from non-optimized melt parameters and spherical pores are artifacts of the powder-manufacturing process, future efforts can be made such that a HIP treatment may be eliminated from the EBM manufacturing process flow. Melt parameters must be optimized to lessen LOF defects, the presence of which can be detected by near-infrared *in-situ* monitoring for qualification purposes [88-90]. In addition, utilization of PREP powder feedstock instead of gas atomized (GA) can result in as-fabricated components manufactured with fewer defects as powders supplied by PREP have fewer gas porosities than GA powders [82]. As-fabricated EBM components do not require heat treatments as they are built at elevated temperatures, effectively eliminating any significant residual stresses [2, 91]. Assuming LOF defects are effectively eliminated using optimized parameters and gas pores held below a minimum threshold using PREP powder, the fatigue strength could be further improved as the fine microstructure, which gives as-fabricated EBM components superior strength to HIP'ed and wrought Ti-6Al-4V, is retained. EBM also allows the opportunities for location specific control of solidification within a single part [92] which can be utilized to further refine and strengthen microstructure in critically-stressed areas.

However, for flight critical components and fatigue applications, a HIP process may be necessary to ensure the LOF melt defects are eliminated and gas pores shrunk to a size that

ensures airworthiness. Although in much smaller quantities than in GA powder, porosity is still observed in PREP powder [82, 93]. Pores in HIP'ed samples were observed in smaller quantities and size than in the as-fabricated condition even if the HIP process is followed by a heat treat [85]. If a pore is sufficiently small, the stress stress/strain concentration zones are in such a small volume of material that a crack is unlikely to initiate and break microstructural barriers [72, 94], and therefore, not expected to influence fatigue behavior [95]. Further work is required to quantify the limits of both pore diameter and percent porosity at which fatigue properties are dominated by microstructure rather than porosity in EBM fabricated Ti-6Al-4V components before an elimination of the HIP process can occur.

5. Conclusions

The microstructure, microhardness, and fatigue behavior of EBM-fabricated Ti-6Al-4V were evaluated as a function of surface finish, internal feature geometry, and build orientation. The following is a summary of the findings:

1. A fine α/β microstructure with colony and Widmanstätten morphologies was observed in the as-fabricated material. Rod-like prior β grains were present as a columnar grain structure was observed in the Z plane along the build direction and a more equiaxed structure in the XY plane parallel to the build plate.

2. Vickers microhardness measurements were consistent across all samples, averaging roughly 335 HVN regardless of wall thickness, build height, and orientation.

3. If present on external surfaces or internal features, surface roughness decreased the fatigue performance. For applications where machining is required, the surface roughness can still decrease the fatigue life unless a sufficient depth (725 μm) of material is removed.

4. Anisotropic fatigue behavior was observed in the four-point bend fatigue tests. In the vertical orientation (where the long axis of the sample is perpendicular to the build plate), the flexural fatigue strength was limited by the inter-layer melt defects that served as early crack-initiation sites. Samples built in the horizontal orientation (long axis parallel to the build plate) displayed comparable fatigue performance to the wrought Ti-6Al-4V, indicating that fatigue is affected by the orientation of LOF melt-related defects.

5. To maximize the fatigue life of a component, it is recommended to eliminate 1) surface roughness by machining and 2) internal defects by a post-fabrication process such as HIP. Note that the HIP process should precede any machining operations, as machining and polishing can expose internal defects to the surface where HIP would be ineffective. Future efforts can be directed to eliminate the need for HIP through optimized melt parameters and building with powder containing fewer gas porosities.

6. When designing for EBM manufacture, limit the scan length below the Arcam recommended length of 90 mm to avoid lack of fusion melt-related defects that can act as fatigue crack initiation sites.

Figures, Tables, and References

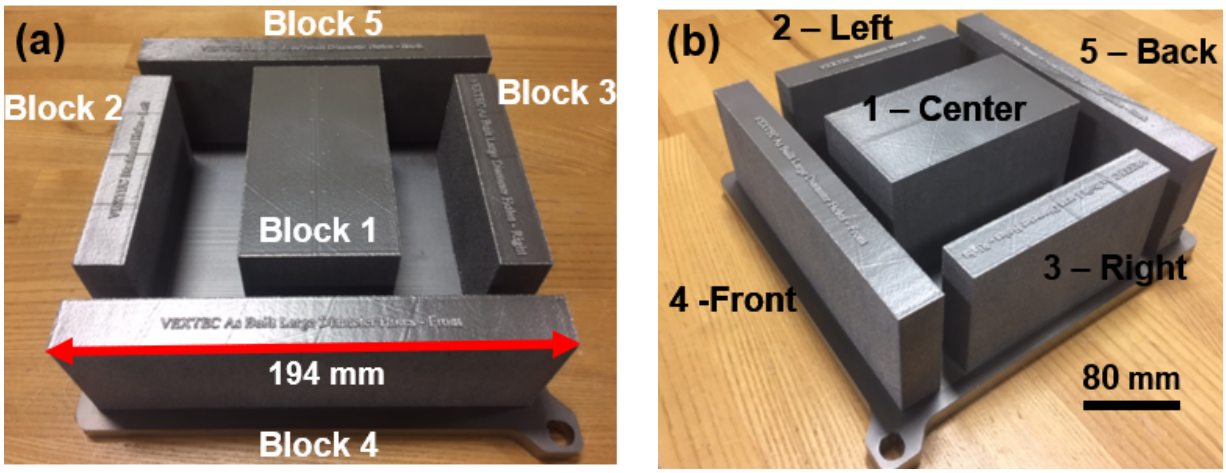

Figure 1. Original EBM build ((a) and (b)) shown prior to machining

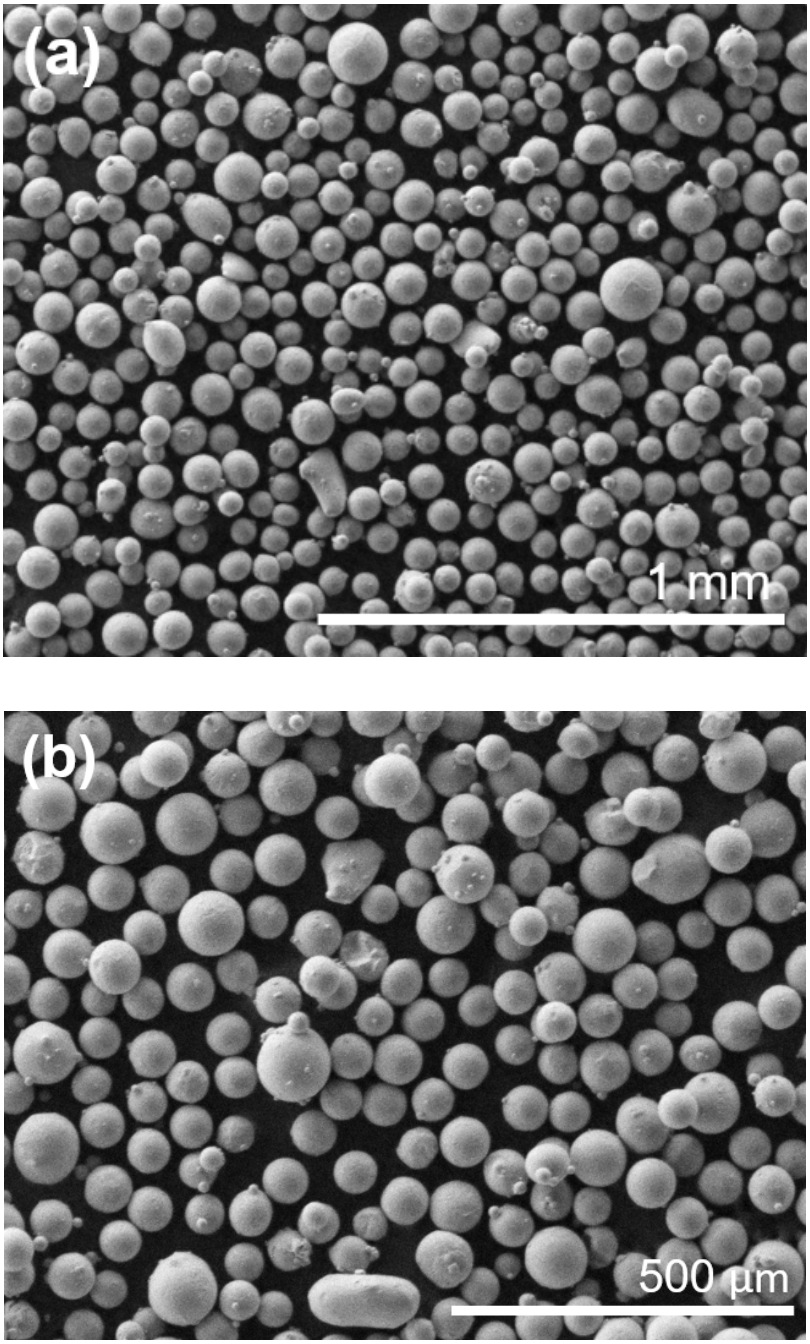

Figure 2. SEM Micrographs of the Ti-6Al-4V powder used in the build at 80x magnification (a) and 120x magnification (b)

Table I. EBM Process Parameters used in the present study

EBM Parameter	Preheat	Outer Contour	Inner Contour	Hatch
Speed (mm/s)	18000	750	800	4530
Max Beam Current for Box (mA)	48	---	---	---
Focus Offset (mA)	44	5	5	32
Beam Pattern	Snake = False	Multi Spot	Multi Spot	Snake = True
Line Order	20	---	---	1
Line Offset (mm)	0.4	---	---	0.2
Size Square (mm)	96	---	---	350 (Split X, Y = 1)
Offset to Part (mm)	4	---	---	---
Spot Time (seconds)	---	0.4	0.8	---
Speed Function	---	6	30	64
Offset (mm)	---	0.22	0.135	---
Beam Current (mA)	---	5	8	15
Max Beam Current (mA)	16 (Jump Safe), 19 (Melt Safe)	5	8	30

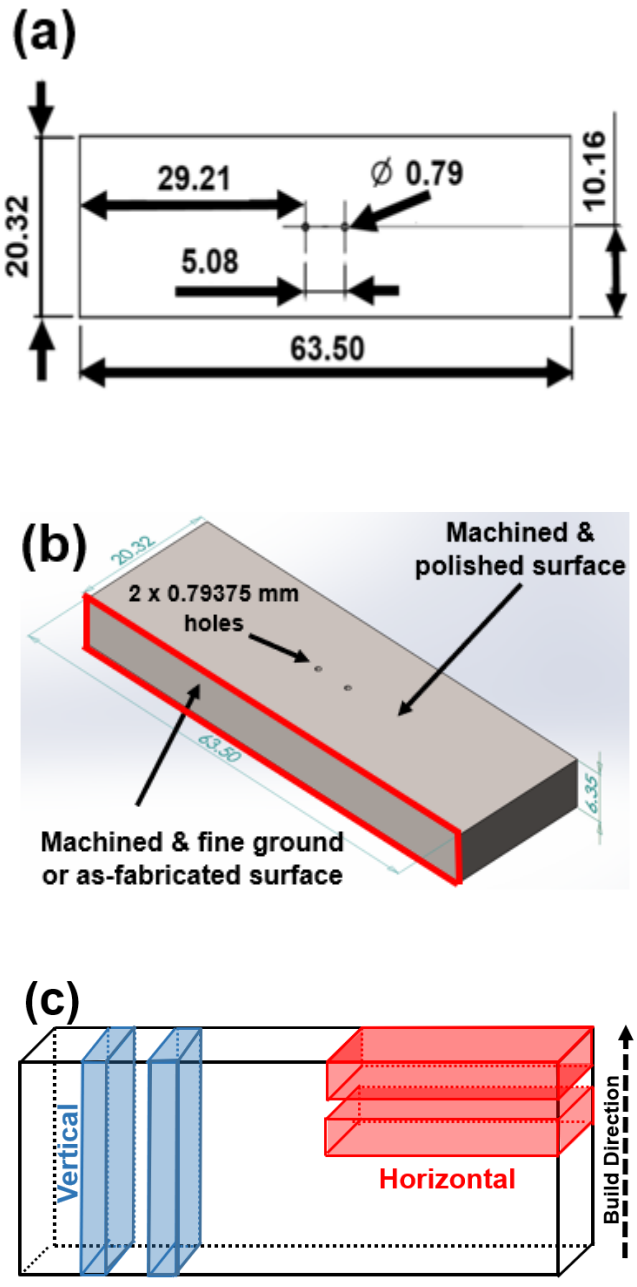

Figure 3. Top-view drawing of fatigue test specimen with dimensions provided in mm (a). Computer model of the four-point bend fatigue test specimen indicating the surface conditions and hole dimensions (b). Schematic indicating how vertical and horizontal fatigue test specimen were machined from original stock material with respect build direction (c)

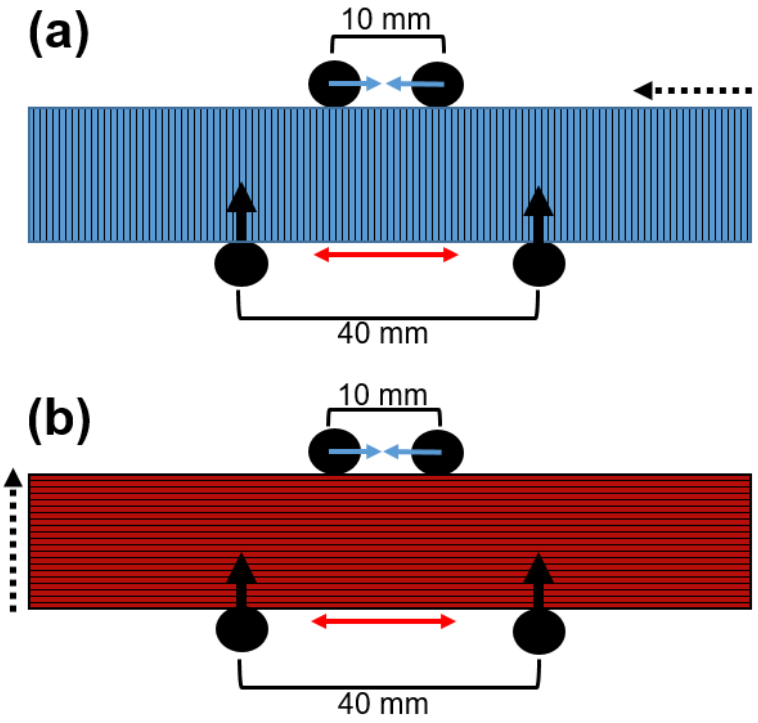

Figure 4. Schematic of experimental 4PB fatigue test set up of both vertically- (a) and horizontally-oriented samples (b). The blue arrows indicate compressive stresses, red arrows tensile stresses, and black solid arrows the loading direction of the bottom pins. The dashed arrows indicate build direction and black lines represent individual build layers.

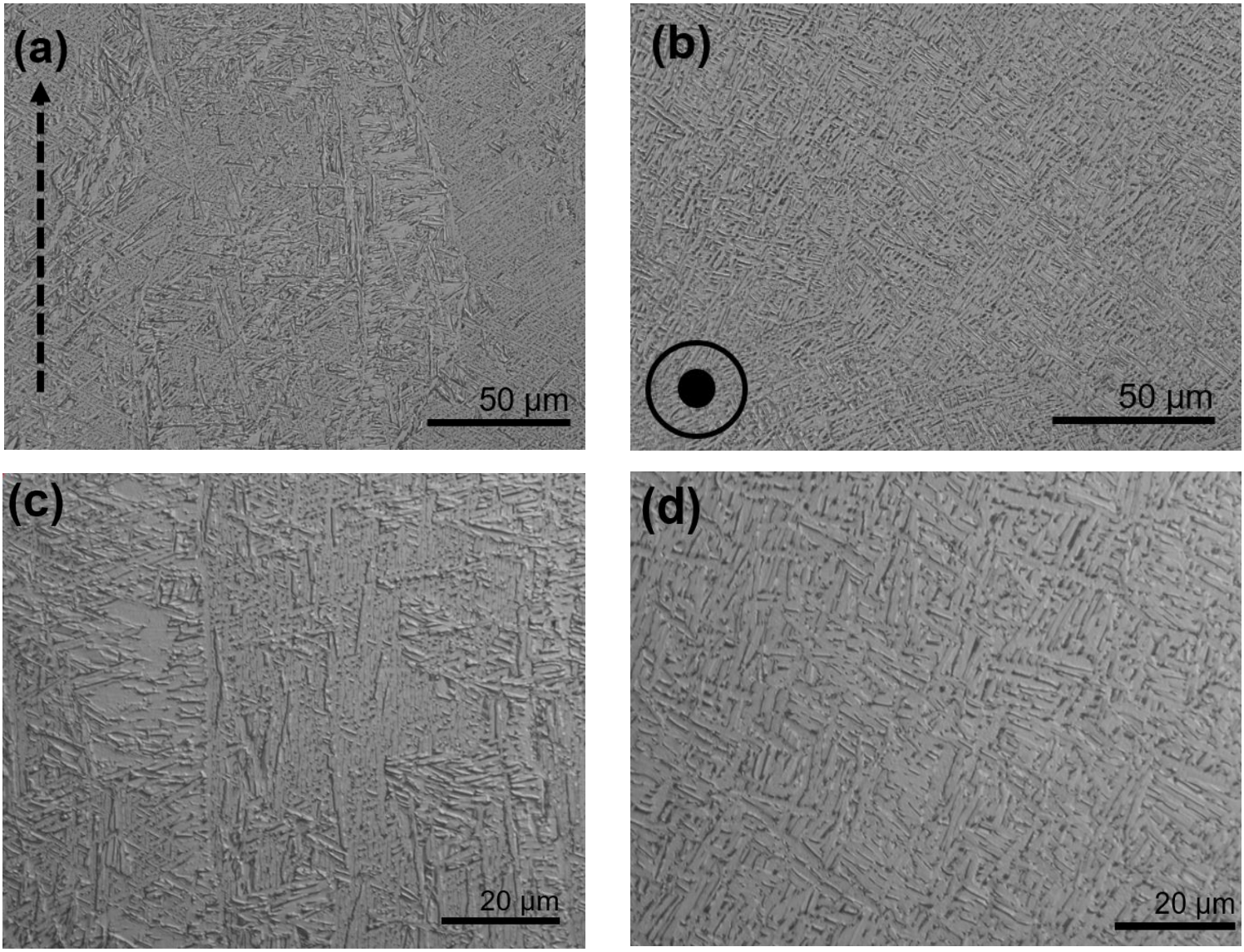

Figure 5. Optical micrographs of EBM Ti-6Al-4V microstructure. The build direction in Figs 5a and 5c is towards the top of the figure. Figs 5b and 5d show the XY plane where build direction is in/out of the page (α - lighter phase, β – darker phase)

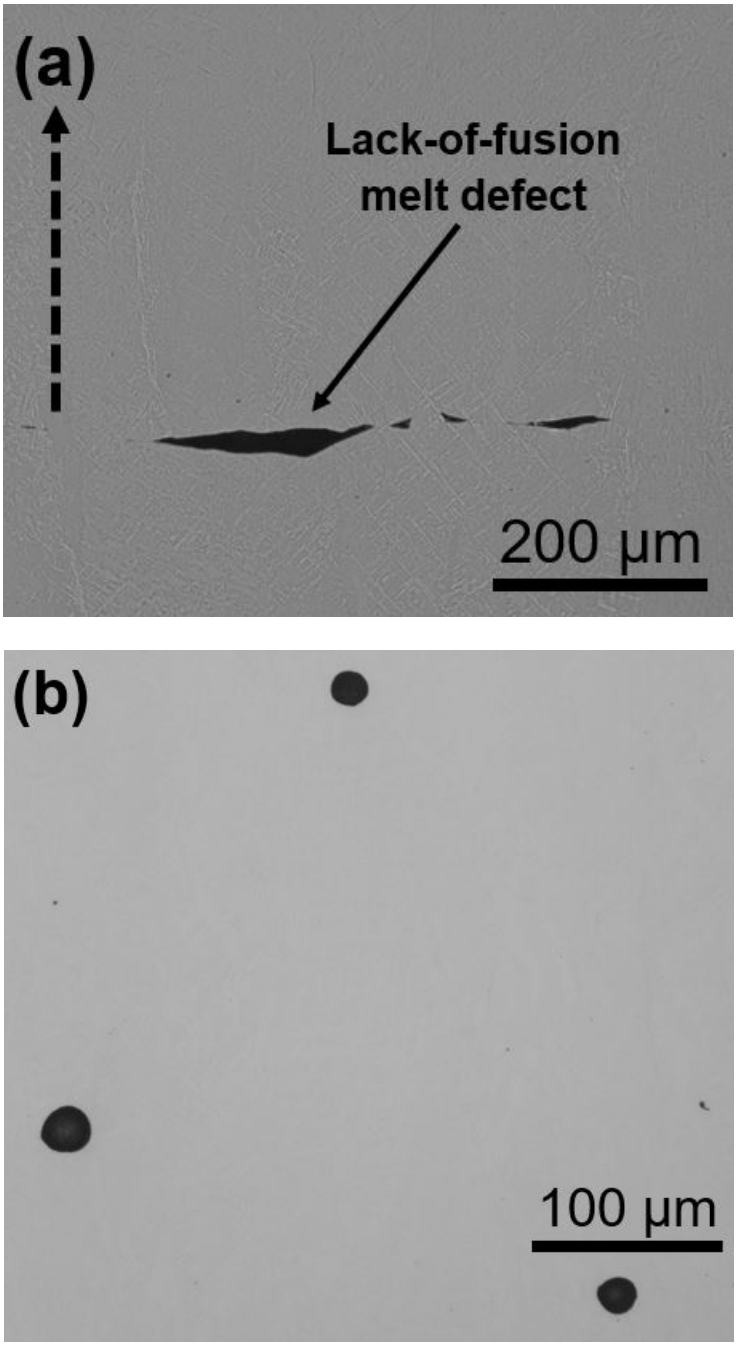

Figure 6. Optical micrographs of common EBM defects: melt-related lack-of-fusion defects oriented perpendicular to build direction (a) and gas porosity (b)

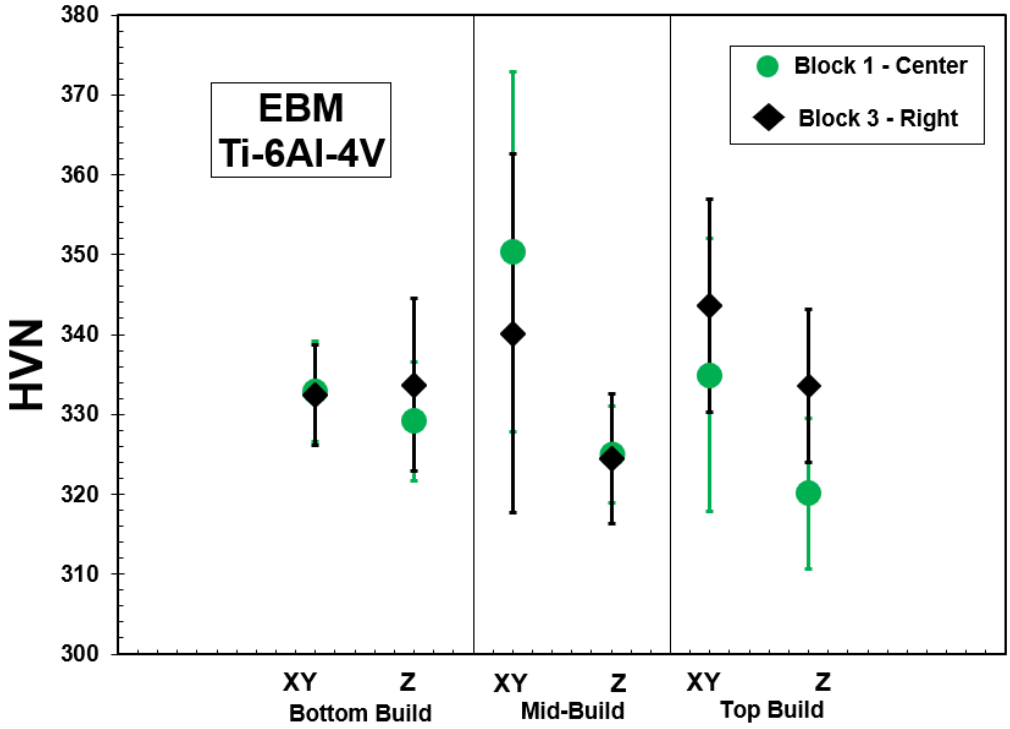

Figure 7. Vickers micro-hardness measurements of EBM Ti-6Al-4V blocks. Error bars correspond to +/- one standard deviation.

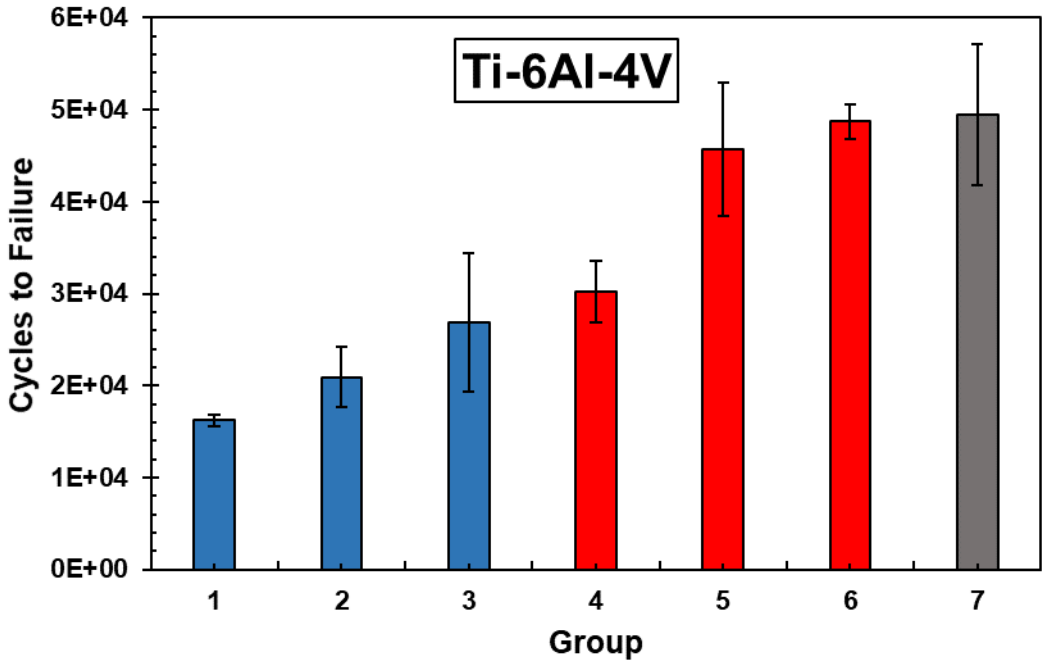

Figure 8. Average fatigue lives of Ti-6Al-4V in various material conditions, surface conditions, and orientations. See Table II for group number descriptions. Blue bars indicate the vertical orientation and red bars indicate the horizontal orientation. Error bars correspond to +/- one standard deviation.

Table II. Summary of experimental four-point bend fatigue results

Group	Orientation	Surface Condition/Hole Condition	Average	Std. Dev.	Stress (MPa)
1	Vertical	As-Built Surface/As-Built Holes	16,195	670	580
2	Vertical	As-Built Surface/Machined Holes	20,920	3,225	585
3	Vertical	Machined Surface/Machined Holes	26,909	7,521	590
4	Horizontal	Machined Surface/Reamed Holes	30,207	3,367	590
5	Horizontal (Block 2)	Machined Surface/Machined Holes	45,759	7,255	590
6	Horizontal (Block 1)	Machined Surface/Machined Holes	48,731	1,856	590
7	Wrought Plate	Machined Surface/Machined Holes	49,464	7,688	590

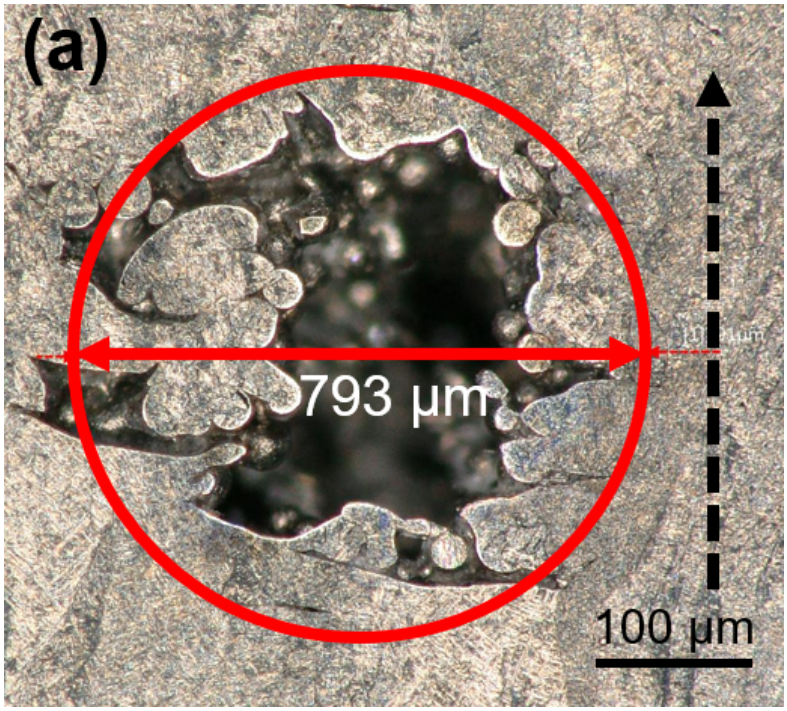

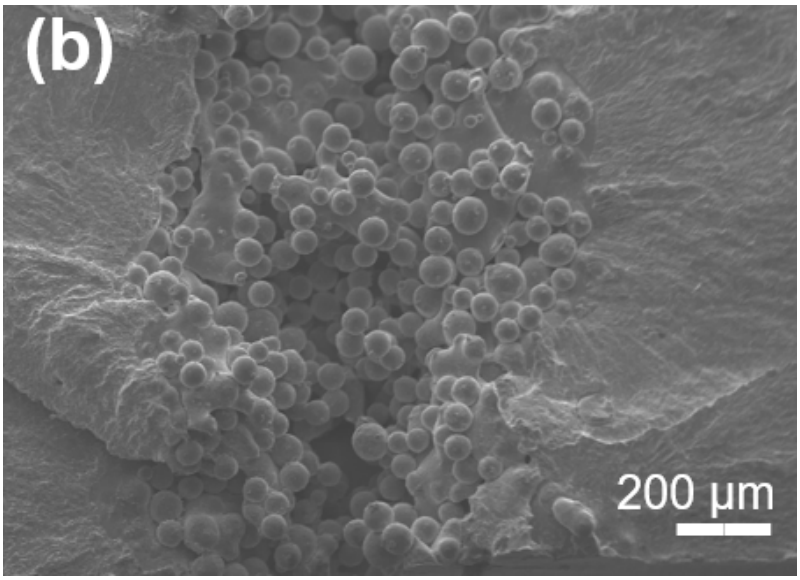

Figure 9. Micrograph of an as-fabricated hole with the designed 793 µm diameter in outlined red (a) and SEM image of the fracture surface of a sample with an as-fabricated hole after fatigue failure (b)

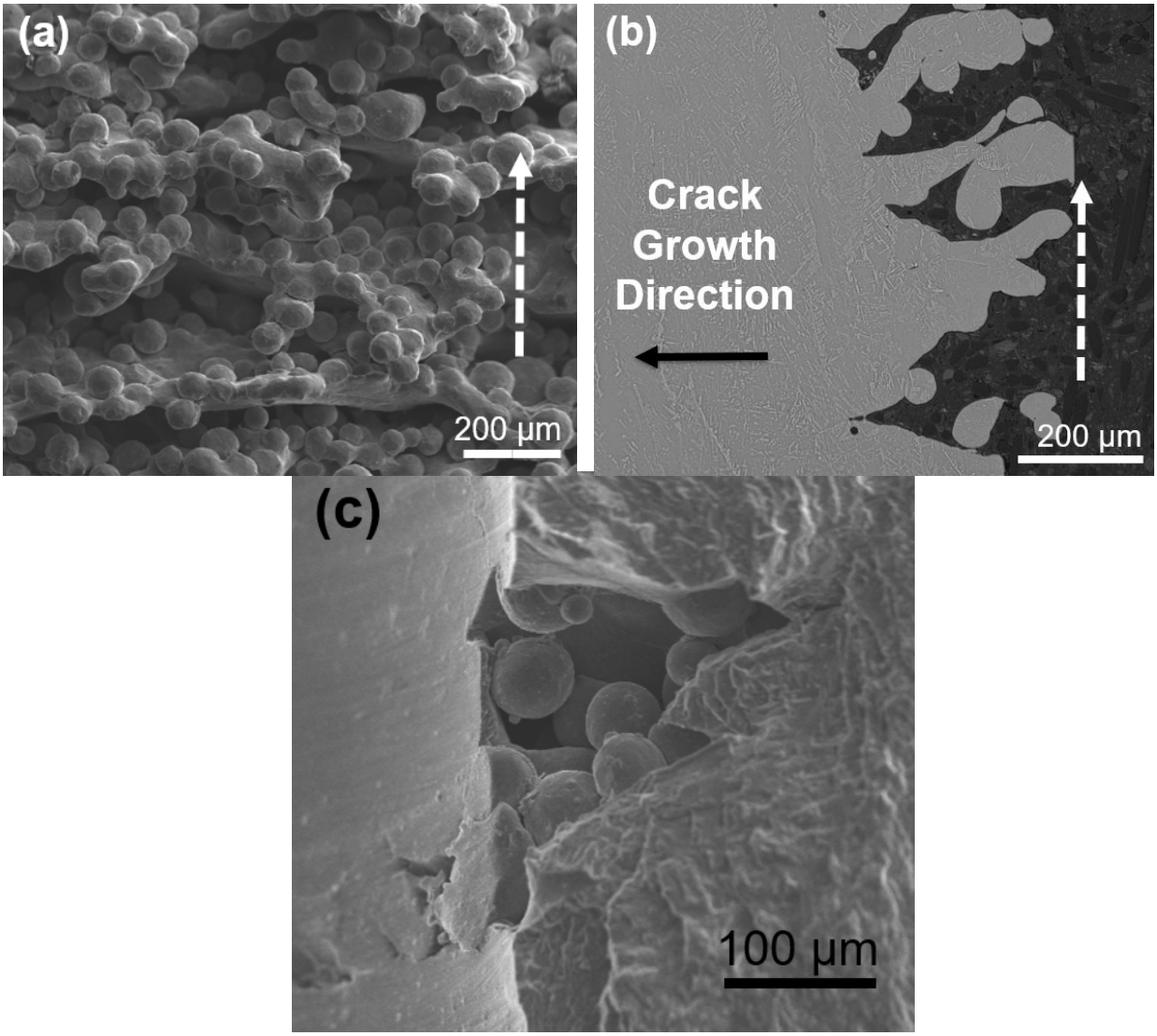

Figure 10. SEM image EBM as-fabricated surface (a), optical micrograph of a surface profile highlighting micro-notches favorable for crack initiation (b), and SEM micrograph of a primary surface roughness defect within the bore of a 'reamed' specimen (c). White dashed arrows indicate the build direction in (a) and (b)

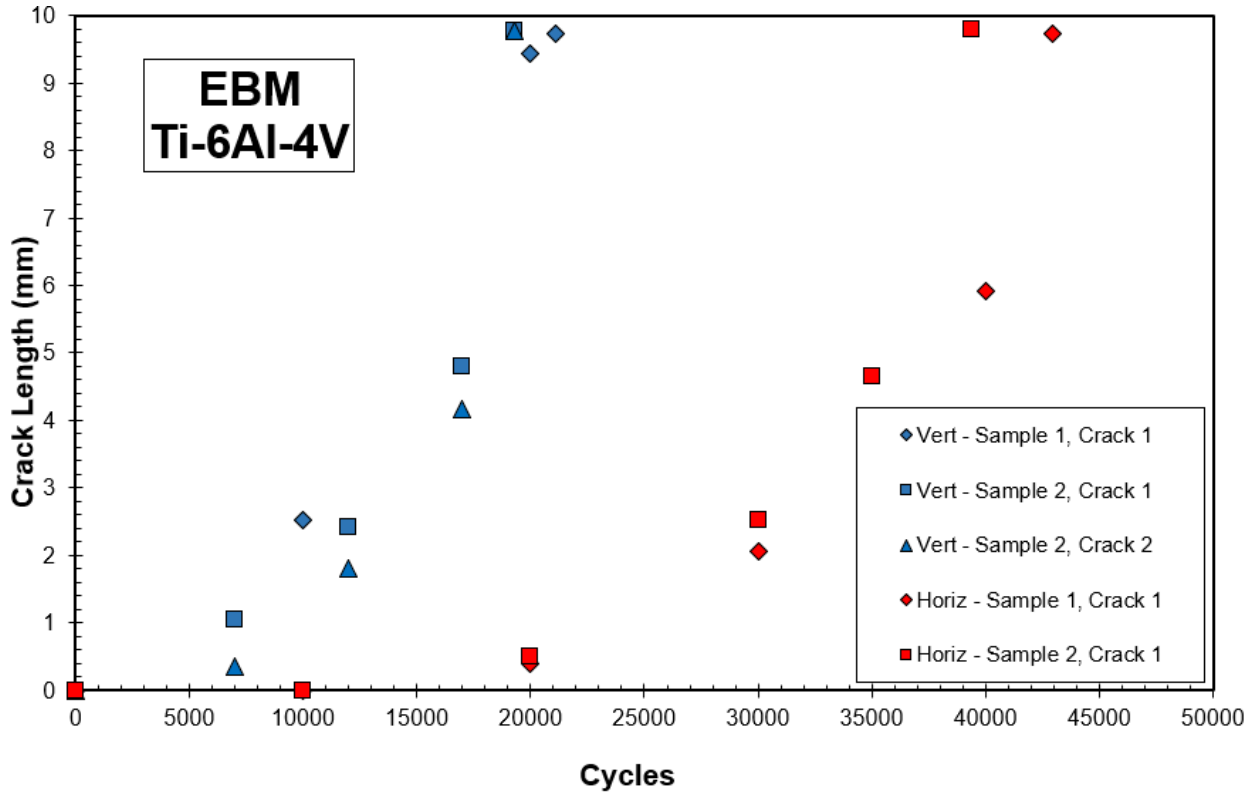

Figure 11. Fatigue crack length as a function of cycle count

Table III. Summary of Interrupted Fatigue Tests

Sample, Crack Number	Fatal Crack Initiation Site	Cycles to Failure
Vertical 1, Crack 1	Surface Defect	21,071
Vertical 2, Crack 1*	Hole×	19,301
Vertical 2, Crack 2*	Hole×	19,301
Horizontal 1, Crack 1	Hole^	42,266
Horizontal 2, Crack 1	Hole^	39,389

*Both cracks observed at the same hole & propagated at nearly symmetric rates
×Multiple cracks observed initiating from surface as well as from hole
^Secondary cracks were not observed from same hole until late (after 30,000 cycles) in the test

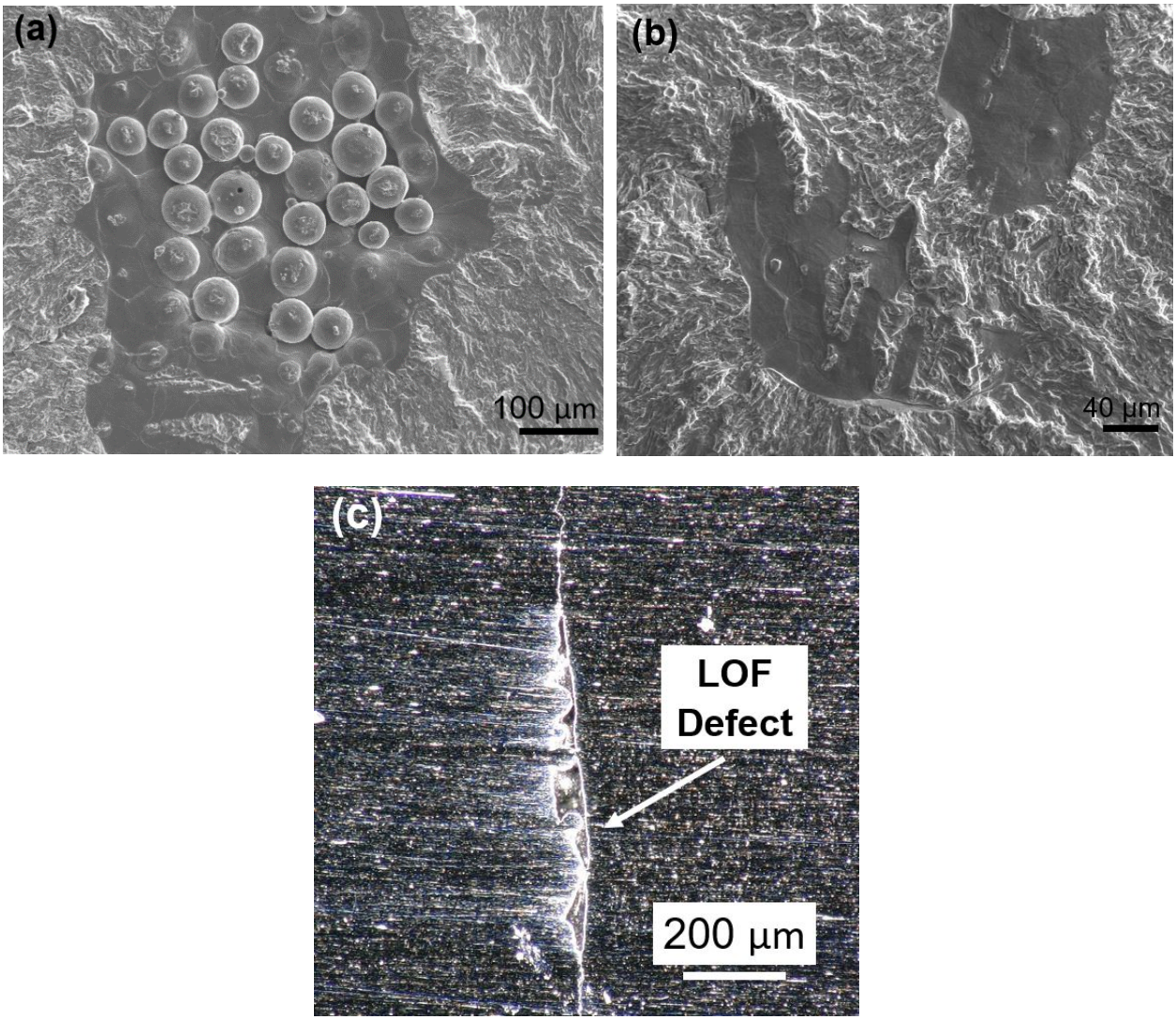

Figure 12. Micrographs of crack-initiation mechanisms in vertical specimen: SEM images of fracture surfaces showing inter-layer LOF defects in (a) and (b), fatigue crack initiating from LOF defect exposed to free surface of a vertical specimen where build direction is right to left (c)

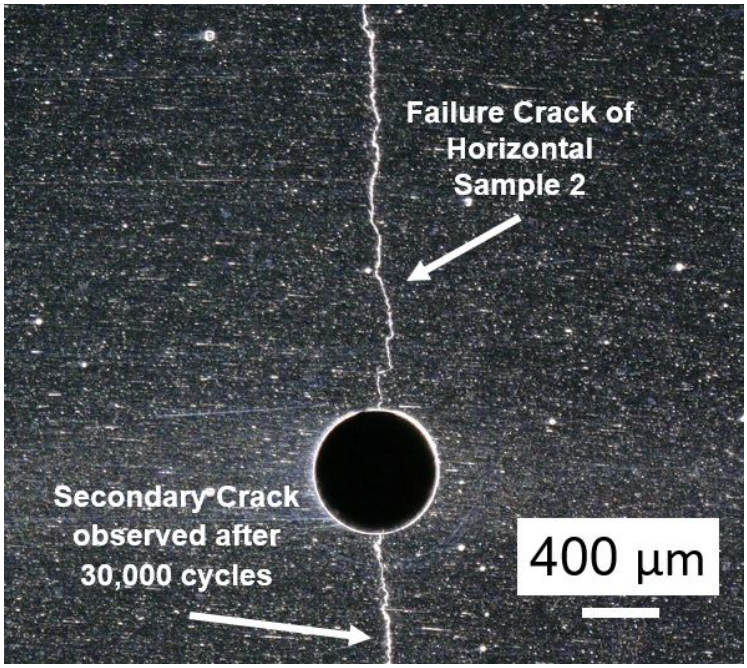

Figure 13. Micrograph of crack-initiation in horizontal specimen. Build direction is in/out of the page

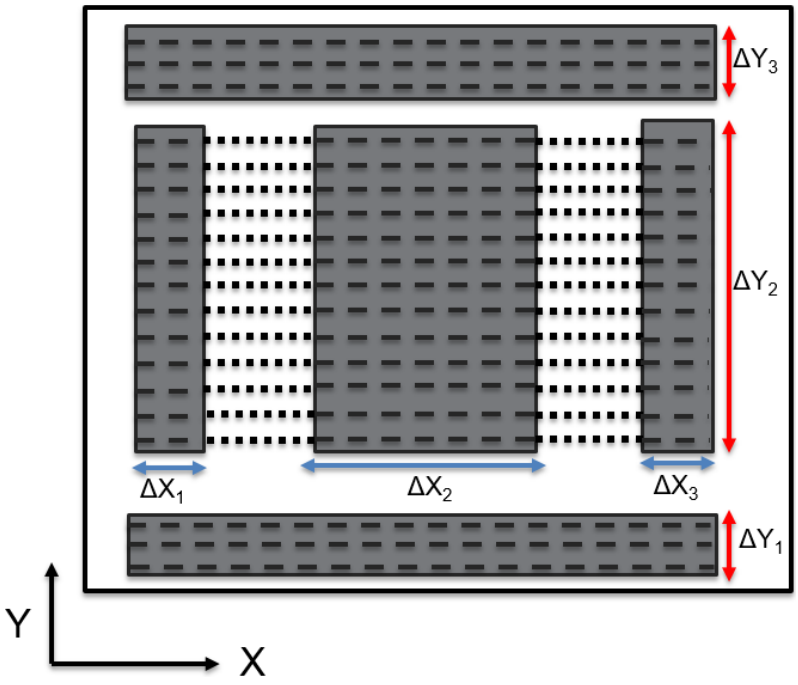

Figure 14. Schematic indicating how a scan length is calculated in EBM Control. In the X direction, the scan length is the sum of ΔX_n values, shown by blue arrows. In the Y direction, the scan length is the sum of the ΔY_m values, shown by red arrows.

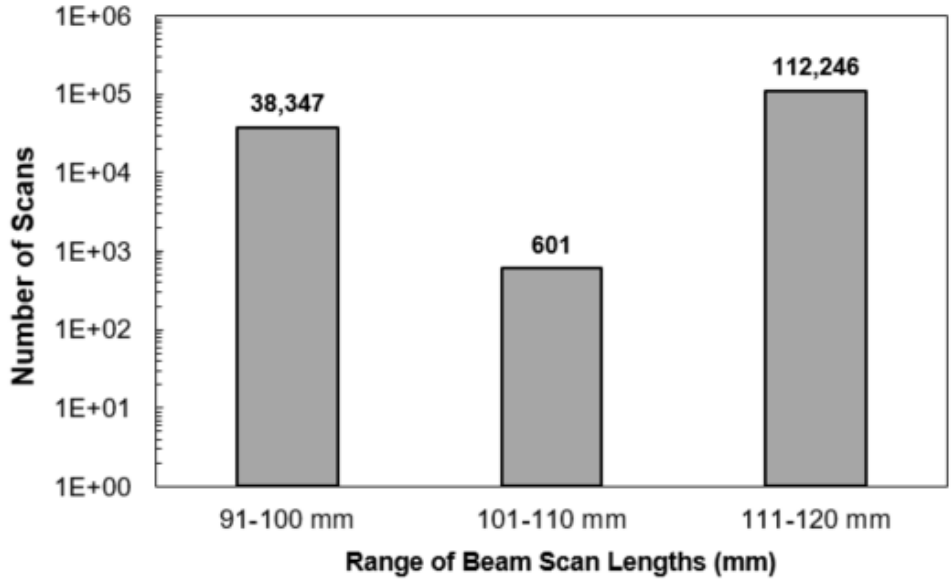

Figure 15. Sum of all beam scan lengths of the specified scan length range throughout the build.

Acknowledgements

Research partially sponsored by the U.S. Department of Energy, Office of Energy Efficiency and Renewable Energy, Advanced Manufacturing Office, under contract DE-AC05-00OR22725 with UT-Battelle, LLC. Research also supported by the Department of the Navy in partnership with VEXTEC. We gratefully acknowledge the support provided through the Navy contract N68335-16-C-0256 and the technical collaboration with Kishan Goel, Madan Kittur, Alan Timmons of NavAir. We would also like to thank Sean Yoder and Dr. Michael M. Kirka of the Manufacturing Demonstration Facility at Oak Ridge National Laboratory for technical expertise, in addition to Zane Palmer and Dr. John Dunlap of the University of Tennessee-Knoxville.

Data Availability

The raw/processed data required to reproduce these findings cannot be shared at this time due to technical or time limitations.

References

1. Jamshidinia, M., L. Wang, W. Tong, R. Ajlouni, and R. Kovacevic, *Journal of Materials Processing Technology*, 2015. **226**: pp. 255-263.
2. Sochalski-Kolbus, L., E.A. Payzant, P.A. Cornwell, T.R. Watkins, S.S. Babu, R.R. Dehoff, M. Lorenz, O. Ovchinnikova, and C. Duty, *Metallurgical and Materials Transactions A*, 2015. **46**(3): pp. 1419-1432.
3. Leyens, C. and M. Peters. 2003: John Wiley & Sons.
4. Lütjering, G. and J.C. Williams. 2007: Springer Science & Business Media.
5. Veiga, C., J. Davim, and A. Loureiro, *Rev. Adv. Mater. Sci*, 2013. **34**: pp. 148-164.
6. Dehoff, R.R., C. Tallman, C.E. Duty, W.H. Peter, Y. Yamamoto, W. Chen, and C.A. Blue, *Advanced Materials and Processes*, 2013. **171**(3): pp. 19-22.
7. Li, P., D. Warner, A. Fatemi, and N. Phan, *International Journal of Fatigue*, 2016. **85**: pp. 130-143.
8. Seifi, M., A. Salem, D. Satko, J. Shaffer, and J.J. Lewandowski, *International Journal of Fatigue*, 2017. **94**: pp. 263-287.
9. Lewandowski, J.J. and M. Seifi, *Annual Review of Materials Research*, 2016. **46**: pp. 151-186.
10. Rafi, H.K., N. Karthik, T.L. Starr, and B.E. Stucker, *Solid Freeform Fabrication Symposium*, 2012: pp. 526-535.
11. ASTM B348-08a, Standard Specification for Titanium and Titanium Alloy Bars and Billets, ASTM International, West Conshohocken, PA, 2008, www.astm.org
12. Al-Bermani, S.S., M.L. Blackmore, W. Zhang, and I. Todd, *Metallurgical and Materials Transactions A*, 2010. **41**(13): pp. 3422-3434.
13. Antonysamy, A.A., J. Meyer, and P. Prangnell, *Materials Characterization*, 2013. **84**: pp. 153-168.
14. Greitemeier, D., F. Palm, F. Syassen, and T. Melz, *International Journal of Fatigue*, 2017. **94**: pp. 211-217.
15. Kahlin, M., H. Ansell, and J. Moverare, *International Journal of Fatigue*, 2017. **101**: pp. 51-60.
16. Edwards, P., A. O'Conner, and M. Ramulu, *Journal of Manufacturing Science and Engineering*, 2013. **135**(6): pp. 061016.
17. Hrabe, N., T. Gnäupel-Herold, and T. Quinn, *International Journal of Fatigue*, 2017. **94**: pp. 202-210.
18. Kirchner, A., B. Klöden, T. Weißgärber, B. Kieback, A. Schoberth, D. Greitemeier, and S. Bagehorn, *Key Engineering Materials*, 2016. **704**: pp. 235-240.
19. Mohammadhosseini, A., D. Fraser, S. Masood, and M. Jahedi, *Materials Research Innovations*, 2013. **17**(sup2): pp. s106-s112.
20. Shui, X., K. Yamanaka, M. Mori, Y. Nagata, K. Kurita, and A. Chiba, *Materials Science and Engineering: A*, 2017. **680**: pp. 239-248.
21. Günther, J., D. Krewerth, T. Lippmann, S. Leuders, T. Tröster, A. Weidner, H. Biermann, and T. Niendorf, *International Journal of Fatigue*, 2017. **94**: pp. 236-245.
22. Chan, K.S., M. Koike, R.L. Mason, and T. Okabe, *Metallurgical and Materials Transactions A*, 2013. **44**(2): pp. 1010-1022.

23. Joshi, G.V., Y. Duan, J. Neidigh, M. Koike, G. Chahine, R. Kovacevic, T. Okabe, and J.A. Griggs, *Journal of Biomedical Materials Research Part B: Applied Biomaterials*, 2013. **101**(1): pp. 124-130.
24. Günther, J., S. Leuders, P. Koppa, T. Tröster, S. Henkel, H. Biermann, and T. Niendorf, *Materials & Design*, 2018. **143**: pp. 1-11.
25. Zhai, T., Y. Xu, J. Martin, A. Wilkinson, and G. Briggs, *International Journal of Fatigue*, 1999. **21**(9): pp. 889-894.
26. Standard Specification for Additive Manufacturing Titanium-6 Aluminum-4 Vanadium with Powder Bed Fusion, West Conshohocken, PA, 2013,
27. Al-Bermani, S.S. 2011, University of Sheffield: Sheffield, UK.
28. Antonysamy, A.A. 2012, The University of Manchester (United Kingdom): Manchester, UK.
29. Sames, W. 2015, Texas A&M University: College Station, Texas.
30. Vander Voort, G. and A. Roosz, *Metallography*, 1984. **17**(1): pp. 1-17.
31. E8, A., *Annual book of ASTM standards. ASTM*, 2001.
32. Chern, A.H., (May 2018), Master's Thesis, University of Tennessee, Knoxville, TN. USA.
33. Hemphill, M.A., T. Yuan, G. Wang, J. Yeh, C. Tsai, A. Chuang, and P. Liaw, *Acta Materialia*, 2012. **60**(16): pp. 5723-5734.
34. Flores, K.M., W.L. Johnson, and R.H. Dauskardt, *Scripta materialia*, 2003. **49**(12): pp. 1181-1187.
35. Aliakbari, M. 2012.
36. Bhavar, V., P. Kattire, V. Patil, S. Khot, K. Gujar, and R. Singh. 2017, CRC Press. pp. 251-253.
37. ASTM F136-13, Standard Specification for Wrought Titanium-6Aluminum-4Vanadium ELI (Extra Low Interstitial) Alloy for Surgical Implant Applications (UNS R56401), ASTM International, West Conshohocken, PA, 2013, www.astm.org
38. ASTM B265-15, Standard Specification for Titanium and Titanium Alloy Strip, Sheet, and Plate, ASTM International, West Conshohocken, PA, 2015, www.astm.org
39. Galarraga, H., D.A. Lados, R.R. Dehoff, M.M. Kirka, and P. Nandwana, *Additive Manufacturing*, 2016. **10**: pp. 47-57.
40. Murr, L., E. Esquivel, S. Quinones, S. Gaytan, M. Lopez, E. Martinez, F. Medina, D. Hernandez, E. Martinez, and J. Martinez, *Materials Characterization*, 2009. **60**(2): pp. 96-105.
41. Seifi, M., M. Dahar, R. Aman, O. Harrysson, J. Beuth, and J.J. Lewandowski, *Jom*, 2015. **67**(3): pp. 597-607.
42. Sames, W.J., F. List, S. Pannala, R.R. Dehoff, and S.S. Babu, *International Materials Reviews*, 2016. **61**(5): pp. 315-360.
43. Tammas-Williams, S., H. Zhao, F. Léonard, F. Derguti, I. Todd, and P. Prangnell, *Materials Characterization*, 2015. **102**: pp. 47-61.
44. Hrabe, N. and T. Quinn, *Materials Science and Engineering: A*, 2013. **573**: pp. 271-277.
45. Kirchner, A., B. Klöden, J. Luft, T. Weißgärber, and B. Kieback, *Powder Metallurgy*, 2015. **58**(4): pp. 246-249.

46. Kok, Y., X. Tan, N. Loh, S. Tor, and C. Chua, *Virtual and Physical Prototyping*, 2016. **11**(3): pp. 183-191.
47. Greitemeier, D., C. Dalle Donne, F. Syassen, J. Eufinger, and T. Melz, *Materials Science and Technology*, 2016. **32**(7): pp. 629-634.
48. Nicoletto, G., R. Konečná, M. Frkáň, and E. Riva, *International Journal of Fatigue*, 2018. **116**: pp. 140-148.
49. Sun, Y., S. Gulizia, C. Oh, D. Fraser, M. Leary, Y. Yang, and M. Qian, *JOM*, 2016. **68**(3): pp. 791-798.
50. Chen, N. and F.V. Lawrence. Vol. 1343. 1999, West Conshohocken, PA: ASTM International.
51. Chan, K.S., *Surface Topography: Metrology and Properties*, 2015. **3**(4): pp. 044006.
52. Young, W.C. and R.G. Budnyas. 2017: McGraw-Hill.
53. Sun, D., D. Keys, Y. Jin, S. Malinov, Q. Zhao, and X. Qin, *Procedia CIRP*, 2016. **56**: pp. 289-292.
54. Zhao, X., S. Li, M. Zhang, Y. Liu, T.B. Sercombe, S. Wang, Y. Hao, R. Yang, and L.E. Murr, *Materials & Design*, 2016. **95**: pp. 21-31.
55. Liu, J., X. Shao, Y. Liu, Y. Liu, and Z. Yue, *Materials Science and Engineering: A*, 2007. **467**(1): pp. 8-14.
56. Abbaschian, R. and R.E. Reed-Hill. 2008: Cengage Learning.
57. Morris, J. 2001, Lawrence Berkeley National Lab.(LBNL), Berkeley, CA (United States).
58. Taha, A. and F. Hammad, *Physica status solidi (a)*, 1990. **119**(2): pp. 455-462.
59. Mitzner, S., S. Liu, M.S. Domack, and R.A. Hafley. in *Solid Freeform Fabrication Symposium*. 2012. Austin, TX.
60. SUI, Y.-w., B.-s. LI, A.-h. LIU, N. Hai, J.-j. GUO, and H.-z. FU, *Transactions of Nonferrous Metals Society of China*, 2008. **18**(2): pp. 291-296.
61. Jamshidinia, M., M.M. Atabaki, M. Zahiri, S. Kelly, A. Sadek, and R. Kovacevic, *Journal of Materials Processing Technology*, 2015. **226**: pp. 264-271.
62. Galarraga, H., R.J. Warren, D.A. Lados, R.R. Dehoff, M.M. Kirka, and P. Nandwana, *Materials Science and Engineering: A*, 2017. **685**: pp. 417-428.
63. Hrabe, N. and T. Quinn, *Materials Science and Engineering: A*, 2013. **573**: pp. 264-270.
64. Tan, X., Y. Kok, Y.J. Tan, G. Vastola, Q.X. Pei, G. Zhang, Y.-W. Zhang, S.B. Tor, K.F. Leong, and C.K. Chua, *Journal of Alloys and Compounds*, 2015. **646**: pp. 303-309.
65. Hornberger, H., C. Randow, and C. Fleck, *Materials Science and Engineering: A*, 2015. **630**: pp. 51-57.
66. Sacristan, I., A. Garay, E. Hormaetxe, J. Aperribay, and P.J. Arrazola, *The International Journal of Advanced Manufacturing Technology*, 2016. **86**(9-12): pp. 2989-3005.
67. Brandl, E., C. Leyens, and F. Palm. in *IOP Conference Series: Materials Science and Engineering*. 2011. IOP Publishing.
68. Keist, J.S. and T.A. Palmer, *Materials Science and Engineering: A*, 2017. **693**: pp. 214-224.

69. Du, D.X., D.X. Liu, Y.F. Sun, J.G. Tang, and X.H. Zhang, *Advanced Materials Research*, 2012. **503-504**: pp. 382-389.
70. Taylor, D., Clancy, O.M., *Fatigue & Fracture of Engineering Materials & Structures*, 1991. **14**(2-3): pp. 329-336.
71. Zhu, L., C. Deng, D. Wang, and S. Hu, *Acta Metall Sin*, 2016. **52**(5): pp. 583-591.
72. Suresh, S. 1998: Cambridge university press.
73. Chern, A.H., P. Nandwana, T. Yuan, M.M. Kirka, R.R. Dehoff, P.K. Liaw, and C.E. Duty, *International Journal of Fatigue*, 2019. **119**: pp. 173-184.
74. Weißmann, V., P. Drescher, R. Bader, H. Seitz, H. Hansmann, and N. Laufer, *Metals*, 2017. **7**(3): pp. 91.
75. Safdar, A., H. He, L.-Y. Wei, A. Snis, and L.E. Chavez de Paz, *Rapid Prototyping Journal*, 2012. **18**(5): pp. 401-408.
76. Persenot, T., J.-Y. Buffiere, E. Maire, R. Dendievel, and G. Martin, *Procedia Structural Integrity*, 2017. **7**: pp. 158-165.
77. Chastand, V., P. Quaegebeur, W. Maia, and E. Charkaluk, *Materials Characterization*, 2018.
78. Gustavsson, B. 2018.
79. Everhart, W., J. Dinardo, and C. Barr, *Metallurgical and Materials Transactions A*, 2017. **48**(2): pp. 697-705.
80. De Formanoir, C., S. Michotte, O. Rigo, L. Germain, and S. Godet, *Materials Science and Engineering: A*, 2016. **652**: pp. 105-119.
81. Persenot, T., A. Burr, G. Martin, J.-Y. Buffiere, R. Dendievel, and E. Maire, *International Journal of Fatigue*, 2019. **118**: pp. 65-76.
82. Chen, G., S. Zhao, P. Tan, J. Wang, C. Xiang, and H. Tang, *Powder Technology*, 2018. **333**: pp. 38-46.
83. Iebba, M., A. Astarita, D. Mistretta, I. Colonna, M. Liberini, F. Scherillo, C. Pirozzi, R. Borrelli, S. Franchitti, and A. Squillace, *Journal of Materials Engineering and Performance*, 2017. **26**(8): pp. 4138-4147.
84. Tammas-Williams, S., P.J. Withers, I. Todd, and P.B. Prangnell, *Metallurgical and Materials Transactions A*, 2016. **47**(5): pp. 1939-1946.
85. Tammas-Williams, S., P. Withers, I. Todd, and P. Prangnell, *Scripta Materialia*, 2016. **122**: pp. 72-76.
86. Tang, H., J. Wang, C. Song, N. Liu, L. Jia, J. Elambasseril, and M. Qian, *JOM*, 2017. **69**(3): pp. 466-471.
87. Cunningham, R., A. Nicolas, J. Madsen, E. Fodran, E. Anagnostou, M.D. Sangid, and A.D. Rollett, *Materials Research Letters*, 2017. **5**(7): pp. 516-525.
88. Mireles, J., C. Terrazas, S.M. Gaytan, D.A. Roberson, and R.B. Wicker, *The International Journal of Advanced Manufacturing Technology*, 2015. **78**(5-8): pp. 1193-1199.
89. Nandwana, P., M.M. Kirka, V.C. Paquit, S. Yoder, and R.R. Dehoff, *JOM*, 2018. **70**(9): pp. 1686-1691.
90. Schwerdtfeger, J., R.F. Singer, and C. Körner, *Rapid Prototyping Journal*, 2012. **18**(4): pp. 259-263.
91. Hrabe, N., T. Gnäupel-Herold, and T. Quinn. in *World Materials Research Institutes Forum International Workshop for Young Scientists*. 2016.

92. Narra, S.P., R. Cunningham, J. Beuth, and A.D. Rollett, *Additive Manufacturing*, 2018. **19**: pp. 160-166.
93. Cunningham, R., S.P. Narra, T. Ozturk, J. Beuth, and A. Rollett, *JOM*, 2016. **68**(3): pp. 765-771.
94. Xu, Z., W. Wen, and T. Zhai, *Metallurgical and Materials Transactions A*, 2012. **43**(8): pp. 2763-2770.
95. Chan, K.S., *International Journal of Fatigue*, 2010. **32**(9): pp. 1428-1447.